Combinatorial Study of Ag–Te Thin Films and Their Application as Cation Supply Layer in CBRAM Cells

Wouter Devulder,*,[†] Karl Opsomer,[‡] Johan Meersschaut,[‡] Davy Deduytsche,[†] Malgorzata Jurczak,[‡] Ludovic Goux,[‡] and Christophe Detavernier[†]

[†]Ghent University, Department of Solid State Sciences, Krijgslaan 281 (S1), 9000 Ghent, Belgium
[‡]IMEC, Kapeldreef 75, 3001 Leuven, Belgium

Ⓢ Supporting Information

ABSTRACT: In this work, we investigate binary Ag–Te thin films and their functionality as a cation supply layer in conductive bridge random access memory devices. A combinatorial sputter deposition technique is used to deposit a graded Ag_xTe_{1-x} $(0 < x < 1)$ layer with varying composition as a function of the position on the substrate. The crystallinity, surface morphology, and material stability under thermal treatment as a function of the composition of the material are investigated. From this screening, a narrow composition range between 33 and 38 at% Te is selected which shows a good morphology and a high melting temperature. Functionality of a single $Ag_{2-\delta}Te$ composition as cation supply layer in CBRAM with dedicated Al_2O_3 switching layer is then investigated by implementing it in 580 μm diameter dot $Pt/Ag_{2-\delta}Te/Al_2O_3/Si$ cells. Switching properties are investigated and compared to cells with a pure Ag cation supply layer. An improved cycling behavior is observed when Te is added compared to pure Ag, which we relate to the ionic conducting properties of Ag_2Te and the preferred formation of Ag–Te phases.

KEYWORDS: Ag–Te, thin films, combinatorial deposition, (in situ) X-ray diffraction, resistive memory, CBRAM
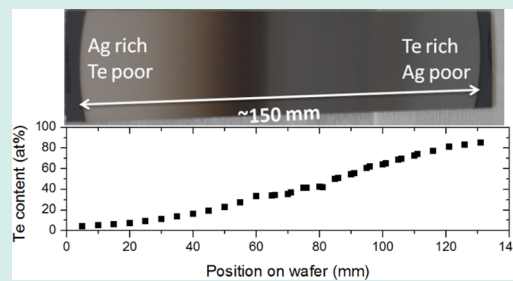
INTRODUCTION

New memory concepts are currently investigated to replace the widely used Flash memory, which is expected to face its scaling limits in the future. Among the emerging technologies, resistive random access memory (RRAM) seems a viable candidate because it combines fast and low power operation with good scalability.[1] In RRAM, a memory element is switched between two resistive states, constituting the on and off or logic 1 and 0 states of the cell. Conductive Bridge Random Access Memory (CBRAM) is a kind of RRAM, and basically consists of an electrochemical active electrode containing Ag or Cu, an electrolyte layer and an inert counter electrode. When a positive bias is applied on the active electrode, cations drift through the electrolyte and are reduced at the counter electrode. A conductive filament of Cu or Ag is grown and when the filament connects both electrodes, the cell switches to a low resistive state (LRS). Applying a bias of opposite polarity dissolves the filament again and switches the cell back to the high resistive state (HRS). In this way reversible switching is possible.[2] Several materials for the electrolyte and active electrode are reported. Chalcogenide materials (Ag_2S,[3] Cu_2S,[4] GeSe,[5] GeS[6]), organic materials[7,8] and binary metal oxides (HfO_2,[9] Ta_2O_5,[10] ZrO_2,[11] SiO_2,[12,13] and Al_2O_3[14]) are reported as electrolyte. For the cation supply layer, besides of pure Cu or Ag, alloys containing these elements have been reported.[15−17] Devices using a chalcogenide material as cation supply layer like Cu_xTe_{1-x}[14] ($x \approx 0.6$), Cu_2S or Cu_2Se[18](or with Ag instead of

Cu) on top of an oxide as switching layer, showed an improved cycling behavior compared to a pure Cu or Ag supply layer. These chalcogenide materials are also reported as solid ionic conductors (SIC).[18,19] From this point of view it is interesting to investigate the binary Ag–Te system, and compare the resistive switching behavior of $Pt/Ag_xTe_{1-x}/Al_2O_3/Si$ CBRAM cells with cells where pure Ag is used. In this paper, we first investigate the material properties of Ag_xTe_{1-x} $(0 < x < 1)$ as a function of the Te content. To allow for efficient material screening, a combinatorial deposition technique is used to create a thin Ag–Te film with a composition that varies as a function of the position on the wafer. Based on material properties, an optimum Ag–Te composition ($Ag_{2-\delta}Te$) is selected to implement in 580 μm diameter dot CBRAM cells and cycling is compared to cells with pure Ag.

EXPERIMENTAL PROCEDURES

To investigate the material properties of Ag_xTe_{1-x} as a function of the composition $(0 < x < 1)$, a 50 nm layer was deposited by magnetron sputtering, using a Balzers deposition tool. The elements are sputtered from two different sputter targets (a pure Ag and a pure Te target), and shadow masks in front of the sputter targets allow to modulate the particle flux and hence

the deposition profile on the substrate. A 150 mm diameter Si wafer passes subsequently in front of each sputter target and in this way a mixed Ag_xTe_{1-x} layer is deposited, with x varying approximately in a linear way from 1 to ~0 in one direction over the 150 mm wafer. Material properties of the layer on different positions on the substrate can then be related to the composition. The thickness of the layer was kept constant to ~50 nm. As substrate, Si(100) wafers covered with a 100 nm SiO_2 or 20 nm thin Al_2O_3 layer are used. The SiO_2 was thermally grown, whereas the Al_2O_3 was deposited by an H_2O-based atomic layer deposition (ALD) technique.

The composition was determined by Rutherford back-scattering spectroscopy (RBS) on different points on the wafer. To this end, 10 nm layers were deposited instead of 50 nm to allow for better distinction between the Ag and Te signal. Composition could also be determined by X-ray fluorescence spectroscopy (XRF) after calibration of the system with a reference sample characterized by RBS. Crystallinity of the film is investigated by X-ray diffraction (XRD). A Bruker D8 Discover X-ray diffractometer, equipped with a 300 mm wafer mapping stage is used for XRD mapping, that is, perform an XRD measurement every 3 mm on the wafer, to investigate the crystallinity as a function of the composition. The system also contains a Mo X-ray source and an XRF detector which is used for the XRF analysis in this work. The morphology of the graded layer is investigated by scanning electron microscopy (SEM), using a FEI Quanta 200F FEG SEM.

The stability of the different Ag−Te phases are investigated using in situ X-ray diffraction, as described in previous work.[17,20] Here, the XRD pattern in a fixed 2θ window of $20°$ is monitored while the sample is annealed at a heating rate of 0.5 °C/s in an inert He atmosphere. In this way, phase transformations as a function of temperature, or the occurrence of melting points are detected. A melt temperature (T_m) higher than 400 °C is necessary to be compatible with back end of line temperatures in device processing.

On the basis of morphology results from SEM imaging and thermal stability observed by in situ XRD measurements, a narrow composition range between 33 and 38 at% Te is selected to implement as cation supply layer in CBRAM cells. We selected the composition with ~64.8 at% Ag, further denoted as $Ag_{2-\delta}Te$. In analogy to previous work,[14,17] cells with a dedicated switching layer of 3 nm Al_2O_3 are used. The alumina is deposited by an H_2O-based ALD process on highly n-doped Si. The CBRAM dot cells are then prepared by magnetron sputtering of a $Pt/Ag_{2-\delta}Te$ (50/50 nm) stack through a 580 μm diameter dot shadow mask on the Al_2O_3/Si substrates. Dots with pure Ag instead of $Ag_{2-\delta}Te$ are also prepared to investigate the influence of the tellurium.

Electrical characterization of the dot cells is carried out with a Keithley 2601A Sourcemeter. Linear current−voltage sweeps with a sweep rate of 0.5 V/s are applied on the Pt top electrode with respect to the Si bottom electrode. The current during the set operation is limited to avoid overgrown filaments. Typically a compliance current (I_c) of 100 μA or 1 mA is used.

■ RESULTS AND DISCUSSION

Combinatorial Study. The composition as a function of the position on the wafer was determined by RBS and the result is shown in Figure 1a. A graded layer with a linearly varying composition from ~0 to ~85 at% Te is obtained. The as-deposited layer is characterized by XRD in the 19−52° 2θ window. The XRD intensities are plotted as a gray scale map as
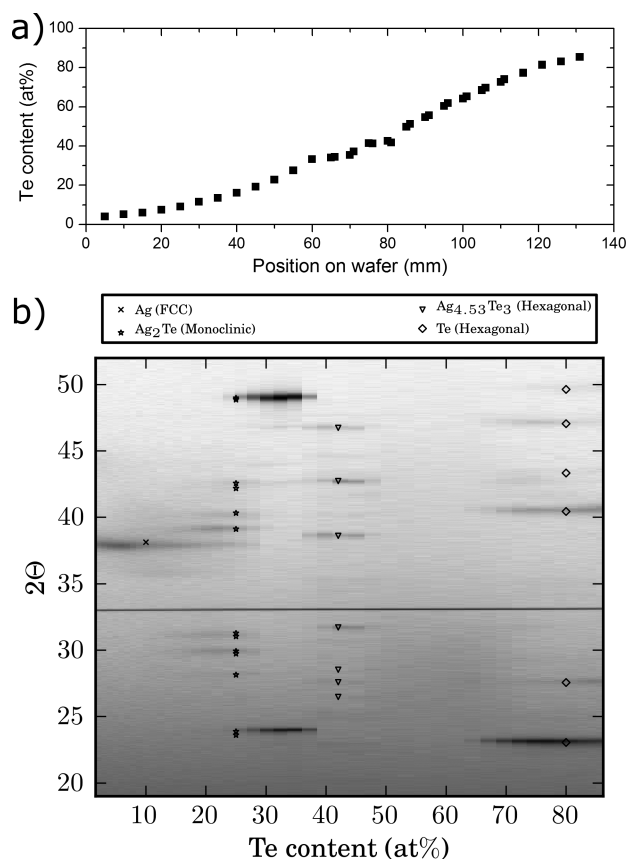

Figure 1. (a) Te content of the Ag−Te layer as a function of the position on the substrate, determined by RBS. (b) XRD patterns as a function of the Te content of the as-deposited layer.

a function of the Te content (Figure 1b). According to the phase diagram,[21] two low temperature intermetallic Ag−Te phases exist, which transform at higher temperatures. In this work, we will follow the notation of ref 21 and denote the low temperature phase with α and the high temperature phases with β, γ, and so on. At a composition of ~33 at% Te, monoclinic Ag_2Te is formed (αAg_2Te), which transforms to a face-centered cubic (fcc) structure at 145 °C (βAg_2Te) and to a body-centered cubic (bcc) structure (γAg_2Te) at 689 °C in case of excess Te (~802 °C in case of excess Ag). At a composition of ~37.5 at% Te, hexagonal Ag_5Te_3 exists ($\alpha Ag_{4.53}Te_3$), which transforms to a high temperature β phase at ~295 °C in case of excess Te (~265 °C for excess Ag). Another phase, $Ag_{1.9}Te$, which exist in the temperature range 120−460 °C, has been reported, with a polymorphic transformation near 178 °C. Unfortunately, to our knowledge, no crystallographic data has been reported on the $Ag_{1.9}Te$ and the high temperature Ag_5Te_3 phases. From the phase diagram,[21] we expect for the as-deposited layer (when it is crystalline) three main regions: (1) 0 to 33.3 at% Te, two phase region with Ag and monoclinic Ag_2Te; (2) 33.3 to 37.5 at% Te, two phase region with monoclinic Ag_2Te and hexagonal Ag_5Te_3; and (3) 37.5 at% Te to pure Te, two phase region with hexagonal Ag_5Te_3 and Te.

This is in agreement with the measured XRD map. Up to about 28 at% Te, the peak corresponding to the [1,1,1] direction of Ag[22] at 38.1° is observed. From 15 to 38 at% Te, also XRD peaks related to the monoclinic Ag_2Te phase[23] appear. In the range ~35 to ~49 at% Te, diffraction peaks of hexagonal $Ag_{4.53}Te_3$[24] are visible. It is apparent that for Te
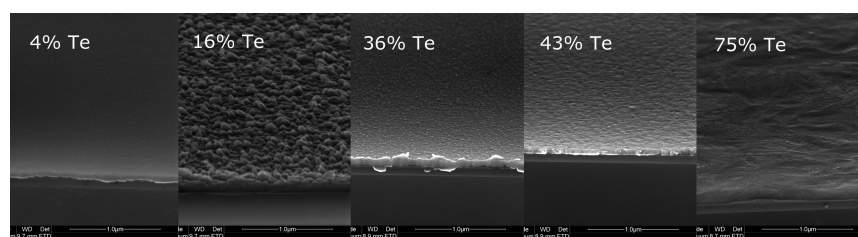
Figure 2. Surface morphology of the ~50 nm Ag–Te layer on 100 nm SiO_2 with 4, 16, 36, 43, and 75 at % Te. The images are taken under a tilted view of 20° and with a magnification of 100 k, the scale bar denotes 1 μm. A strong variation in surface roughness is observed.

contents in the range of 29–38 at% Te mainly two peaks are very intense, corresponding to the [−1,2,1] direction of monoclinic Ag_2Te ([−1,2,1] and [−2,4,2] at respectively 23.9° and 48.8°). For Te contents higher than 65 at%, peaks related to tellurium[25] are present. The material in the composition region between 49 and 65 at% Te, where no diffraction peaks appear, is probably amorphous.

Figure 2 shows the SEM images of the main composition regions. The surface morphology is strongly dependent on the Te content. For almost pure Ag, a smooth morphology is observed, whereas adding more Te creates a rough surface (e.g., for 16 at% Te in Figure 2). At the Ag rich side of Ag_2Te (<33 at % Te), large particles are observed which are related to the excess of Ag (see also Figure S2b in the Supporting Information), whereas at the Ag poor side (>33 at% Te) where only intermetallic Ag–Te phases or Te (>65 at% Te) occur, a smooth surface morphology is present. These results suggest that an excess of Ag that cannot be consumed in intermetallic phases results in a rough surface morphology and Ag particles. Only pure Ag or materials with more than 33 at% Te show good as-deposited surface morphologies.

The thermal stability of the Ag–Te layer as a function of the Te content was further investigated using in situ XRD. The graded wafer was cleaved into pieces of about 7 mm and hence for 18 different compositions, a measurement is available. Figure 3 shows selected results for significantly different composition regions, as the regions in between show qualitatively similar patterns. The composition of every piece before and after the in situ XRD was measured by XRF to investigate whether the composition had changed during the anneal (for example by evaporation). Figure 4a shows a summary of the temperature windows where the different intermetallic phases appear as a function of the initial (i.e., before anneal) Te composition. The temperatures where these phases appear/disappear were extracted based on the appearance/disappearance of the corresponding diffraction peaks in the 30–50° 2θ window. The composition after the measurement is also indicated.

Figure 3a shows the result for a layer with almost pure Ag (only 4 at% Te). Indeed, only the [1,1,1] peak at 38.1° is visible as deposited, and the diffraction peak appearing from 200 °C on at 44° corresponds to the [2,0,0] peak of Ag.[22] Adding more Te results in the formation of the monoclinic Ag_2Te phase,[23] as is illustrated in Figure 3b for 28 at% Te. Near a temperature of 145 °C, the peaks assigned to the monoclinic Ag_2Te phase disappear, which can be explained by the α- to βAg_2Te[26] phase transformation from a monoclinic to a fcc structure.[21] The sample with a composition around 37 at% (Figure 3c) is the most difficult to analyze. For temperatures below 145 °C the [−2,4,2] peak of monoclinic Ag_2Te is visible. According to the phase diagram, one also expects hexagonal $Ag_{4.53}Te_3$,[24] but no
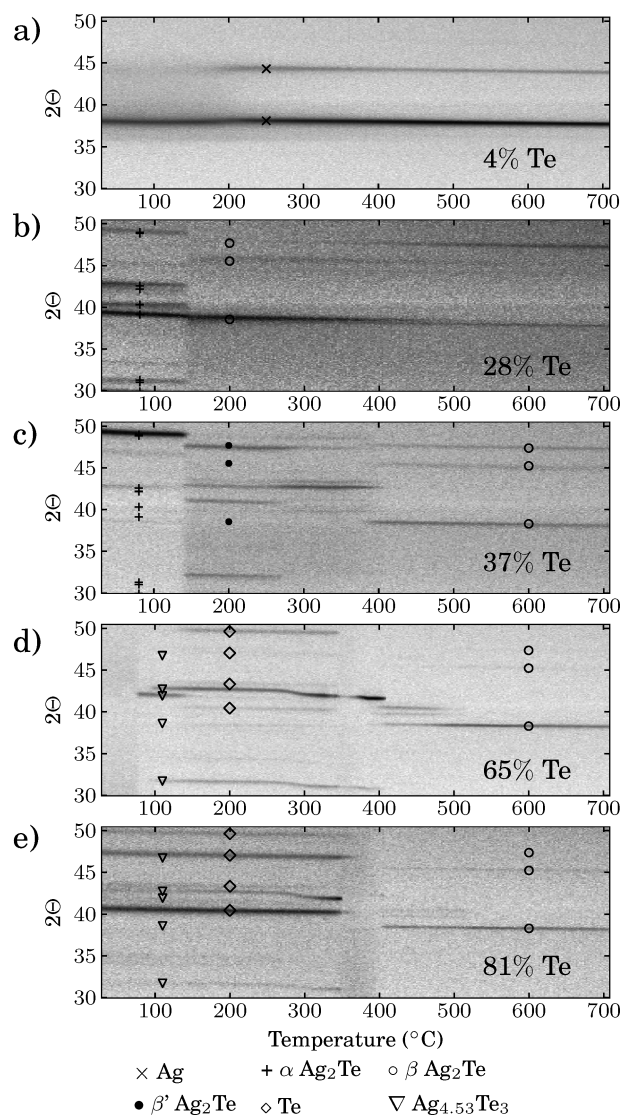

Figure 3. In situ XRD patterns of the graded Ag–Te layer on 20 nm Al_2O_3 for the regions with (a) 4, (b) 28, (c) 37, (d) 65, and (e) 81 at% Te. The diffraction peaks are plotted as a gray scale map as a function of the temperature.

diffraction peaks of this phase are observed. The phase diagram also mentions a high temperature $Ag_{1.9}Te$ phase in the 120–460 °C temperature window, which exists in two polymorphs with a transformation temperature of 178 °C.[21] The in situ XRD measurement shows that at 145 °C the monoclinic phase transforms, followed by an apparently second transformation around 265 °C, where the peaks at 32° and 41° disappear, and the peak at 42.7° becomes more intense. The diffraction peak at
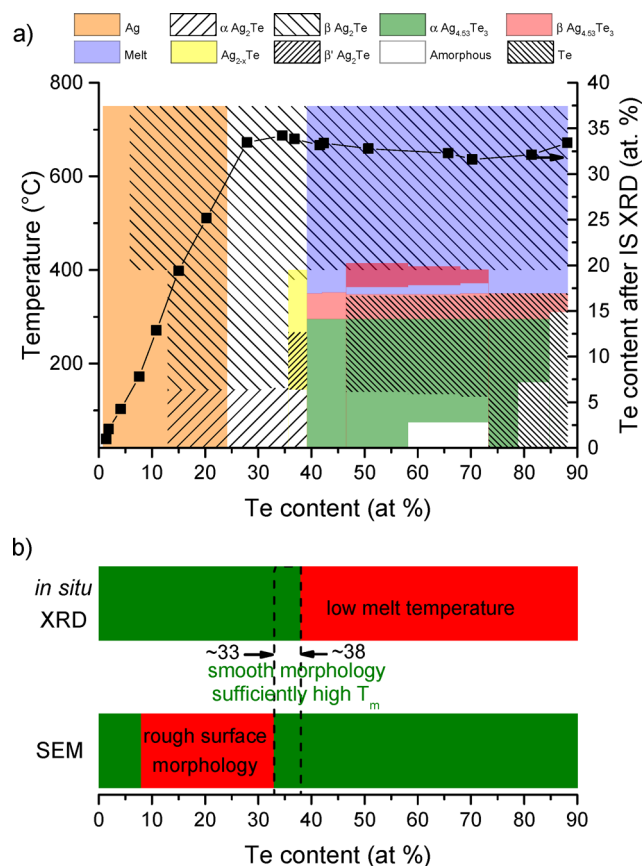
a)

b)

Figure 4. (a) Summary of the observed phases in the 30−50° 2θ window. The temperature window where a certain phase appears as a function of the composition is hatched in the diagram. The composition after the in situ XRD measurement is also indicated. (b) Summary of the material properties investigated by in situ XRD and SEM.

42.7° becomes less intense only at 280 °C. At 400 °C, the peak at 42.7° disappears and diffraction peaks corresponding to fcc Ag_2Te appear.[26] To investigate this composition further and to identify the observed XRD peaks, a Ag−Te layer with 63.9 at% Ag was deposited. The in situ XRD measurement is very similar to the observed one of the gradient (Figure 3c) and is shown in Figure S1 in the Supporting Information. For this sample, also a second 2θ window was measured. The two 2θ windows in Supporting Information Figure S1 show that at 145 °C two intense peaks at 23.3 and 47.7° appear, which can be related to the [1,1,1] and [2,2,2] planes of fcc Ag_2Te.[27] Additional measurements where the sample was annealed up to 220 and 390 °C and cooled down to room temperature again were performed to investigate if the phases at that temperature are also stable at room temperature. Upon cooling, the present peaks shifted toward larger 2θ angles (which could be explained by thermal expansion) but also more diffraction peaks appeared which could be related to the monoclinic phase. These results suggest that the diffraction peaks formed above 145 °C are merely high temperature phases that return to a low temperature phase at room temperature, and support the proposition that cubic Ag_2Te[26,27] appears from 145 °C on. Other diffraction peaks appearing in the 145−400 °C temperature window are hard to identify, and might be related to other high temperature phases like $Ag_{1.9}Te$. Unfortunately no reference XRD data is available for the $Ag_{1.9}Te$ phase in the

literature. Note that literature even reports the existence of a second medium temperature Ag_2Te phase[28] in the temperature range 146−260 °C. In Figure 4, the occurrence of unidentified peaks are taken into account under the general notation of $Ag_{2−x}Te$. Also two notations (β and β') are used for the high temperature Ag_2Te phase, which only differ in the lattice constant.

When more than 38 at% Te is present, the material has a melting point around 350 °C, as can be seen in Figures 3d and e for respectively 65 and 81 at% Te. In case of 65 at% Te, the material is amorphous as deposited, and the hexagonal $Ag_{4.53}Te_3$ phase crystallizes at 75 °C. Around 295 °C, the diffraction peaks at 42.7 and 31.7°, corresponding to the [0,0,6] and [0,0,8] planes, shift toward 42° and 31°, respectively. Although no reference XRD data is available to verify, this temperature coincides with the reported α to β transition[21] of $Ag_{4.53}Te_3$. At 350 °C, the diffraction peaks disappear, corresponding to the melting temperature of the eutectic composition. At higher temperatures, diffraction peaks appear again, which can be explained by evaporation of Te. In this way, the material becomes Ag rich and solid phases (Ag_2Te) appear again. This is also in agreement with the measured composition after the in situ XRD measurement: for the samples where fcc Ag_2Te is formed, the composition is about 66 at% Ag (see Figure 4a). As we cannot exactly determine at which temperature no liquid is present anymore, we indicated in Figure 4a the whole temperature range above 350 °C as a region where liquid can occur. For the sample with 81 at% Te, diffraction peaks associated with Te are clearly visible. On the basis of these results, the composition range with more than 38 at% Te is excluded for memory application because of the low T_m of 350 °C. Figure 4b summarizes the composition regions selected by the combinatorial screening with good surface morphology (selected from SEM screening) and sufficiently high melting temperature (selected from in situ XRD).

Optimum Composition: $Ag_{2−\delta}Te$. The combinatorial screening in the previous section allowed us to select a narrow composition range with acceptable material properties between 33 and 38 at% Te. For too low Te compositions, a rough surface morphology was observed whereas for too high Te contents, the material melts already at 350 °C. This is also illustrated in Figure 4b, where the regions with good surface morphology and sufficiently high melting temperature overlap. A composition close to Ag_2Te was selected, and at the Ag deficient side, to avoid the rough surface morphology. The composition was determined by XRF as 64.8 at% Ag and we will further refer to this composition as $Ag_{2−\delta}Te$. A slight excess of Ag results in large Ag grains on the surface. This was confirmed by energy dispersive X-ray fluorescence spectroscopy (EDX) on a sample with 70 at% Ag. This is illustrated in Figure S2 in the Supporting Information, showing the SEM images of both compositions. The in situ XRD measurement of $Ag_{2−\delta}Te$ (see Supporting Information Figure S3a) shows only the α to βAg_2Te transformation, whereas for the layer with 70 at% Ag (Supporting Information Figure S3b), also diffraction peaks corresponding to Ag appear. For temperatures above 145 °C, βAg_2Te exists, but it is observed from in situ XRD that it transforms back to αAg_2Te upon cooling. The ionic conductivity is also higher for βAg_2Te[28] (the high temperature phase) compared to αAg_2Te.[29]

Application in CBRAM. The DC cycling behavior of Pt/ $Ag_{2−\delta}Te/Al_2O_3/Si$ dot cells is compared to cells with pure Ag as a cation supply layer. The cells are cycled 10 times by

applying a double linear voltage sweep from 0 to 3 V (and back) to set the cells to a LRS, and from 0 to −2.5 V (and back) to reset them into a HRS. Figure 5 shows typical
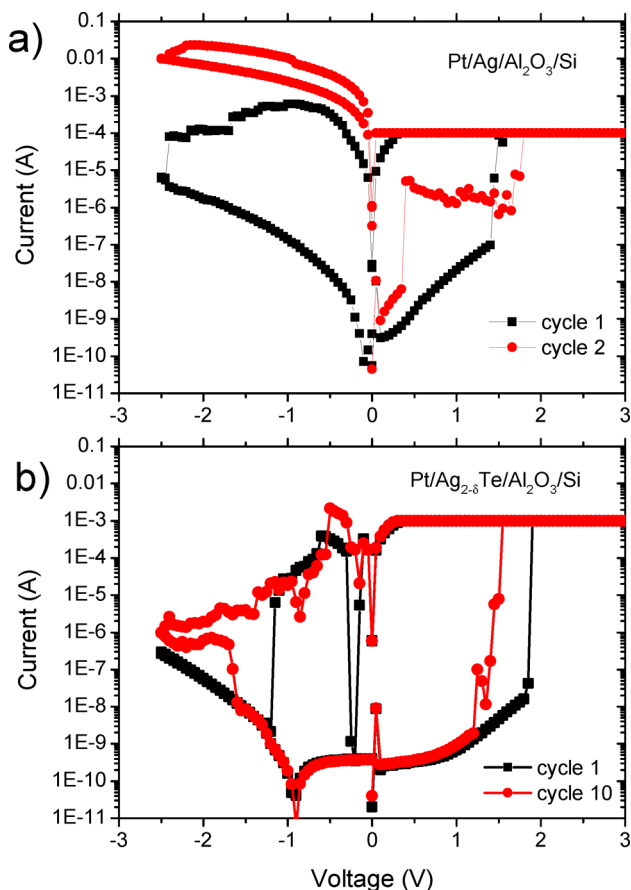

Figure 5. DC sweeps of (a) Pt/Ag/Al$_2$O$_3$/Si and (b) Pt/Ag$_{2-\delta}$Te/Al$_2$O$_3$/Si CBRAM cells.

switching curves for both supply layers. The cells with Ag (Figure 5a) show a forming, that is, Ag ions are driven into the Al$_2$O$_3$ switching layer to form a conductive filament and the cell is switched to a LRS during the first cycle, but it is difficult to reset the cells. Using Ag$_{2-\delta}$Te on the other hand (Figure 5b) resulted in better cycling of the cells. In the case of Ag, the current was limited to 100 μA to avoid a too strong filament, as a higher compliance current generally leads to stronger filaments.[5] In case of Ag$_{2-\delta}$Te, the cells can even be reset when a I$_c$ of 1 mA was used during set. This efficient reset for the Te alloyed supply layer was already reported for Cu−Te,[14] but also for Cu or Ag based sulfides and selenides with a binary oxide as switching layer.[18] It is known that the copper[4,19] and silver[28,29] chalcogenides show ionic conductivity. It is very likely, as was proposed previously,[18,30,31] that the good ionic conductivity of the supply layer allows for the efficient reset because of a more efficient flux of ions out of the switching layer back into the supply layer during reset. A better extraction of the Ag ions out of the switching layer is expected to contribute to the recovery of the high resistive state and hence to an efficient reset. Another factor that might play a role is the thermodynamical driving force to form intermetallic Ag−Te phases. When a Ag filament is formed in the Al$_2$O$_3$ layer during the set operation, a Te rich region is left in the silver supply layer. However, as it is thermodynamically more favorable for

Ag to form Ag−Te phases, the Ag atoms constituting the conductive filament will tend to go back to the Te rich region in the supply layer, which should contribute to filament dissolution and hence reset.[14]

It is observed that for Ag$_{2-\delta}$Te a compliance current of 1 mA is needed to obtain a stable filament that does not dissolve spontaneously or with very low reset voltages. This is illustrated in Figures 6a and b, where the cumulative distribution of the resistances of the Ag$_{2-\delta}$Te cells are extracted from the set (read at +0.1 V) and reset (read at −0.1 V) cycles. In the ideal case, the curves at positive and negative read voltage should coincide. Using an operating current of 100 μA (Figure 6a) results in ~50% of the switches where the LRS returned already to a higher resistance at −0.1 V, and about 15% returned to a HRS (i.e., $R > 10^6 \Omega$). Using a compliance current of 1 mA (Figure 6b) results in much more successful cycles, that is, 90% of the programmed LRS are still in the same state during reset at −0.1 V and only ~1% returned to a HRS again. As is generally observed in CBRAM, a higher compliance current generally leads to stronger and hence less volatile filaments. This agrees with the more stable LRS for the cells cycled with 1 mA because of the thicker filaments that contain more silver atoms. Note that the influence of filament morphology on retention has been reported before,[32] where better retention is reported for LRS states with lower resistance because of thicker filaments, which are less susceptible to filament dissolution. From the cumulative plots, it is also observed that a larger fraction of the LRS states has a lower LRS resistance for the cells cycled with 1 mA compared to the cells cycled with 100 μA, illustrating the more robust filament for the former. It is worth mentioning that the Joule heating because of the high current that flows through the filament might induce the α to βAg$_2$Te phase transition in the Ag−Te layer close to the filament when temperatures above 145 °C are reached. However, not much information on the phase transformation and existence of the high temperature phase on this local scale is known. Moreover, when no current flows through the cell and the material cools down, this phase is expected to transform back to the low temperature α phase. In case that βAg$_2$Te is formed, this might enhance the flux of Ag ions out of the silver supply layer when the cell has switched on during the set sweep, as a higher ionic conductivity is reported for the cubic high temperature phase.[28,29] This in turn can promote a more robust, thicker filament that contains more Ag atoms, which improves LRS stability. During reset, the higher ionic conductivity of the cubic phase might enhance the flux of Ag ions out of the Al$_2$O$_3$ back into the Ag−Te layer, and hence contribute to the efficient reset. Endurance of the 580 μm Ag−Te based dot cells was also tested by DC cycling of the cells with a I$_c$ of 1 mA. Figure 6c shows the resistance of 500 consecutive set-reset cycles, extracted from a 100 mV read pulse after every set or reset operation.

■ CONCLUSIONS

We deposited a 50 nm thin film of Ag$_x$Te$_{1-x}$ ($0 < x < 1$) by a combinatorial deposition technique and investigated the material properties as a function of the composition. SEM measurements revealed a rough surface morphology when the Ag$_2$Te phase was formed with an excess of Ag, whereas a smooth morphology is observed when more Te is added and all Ag is consumed in intermetallic phases. X-ray diffraction mapping shows the formation of intermetallic Ag−Te phases, in agreement with the phase diagram. In situ XRD as a function
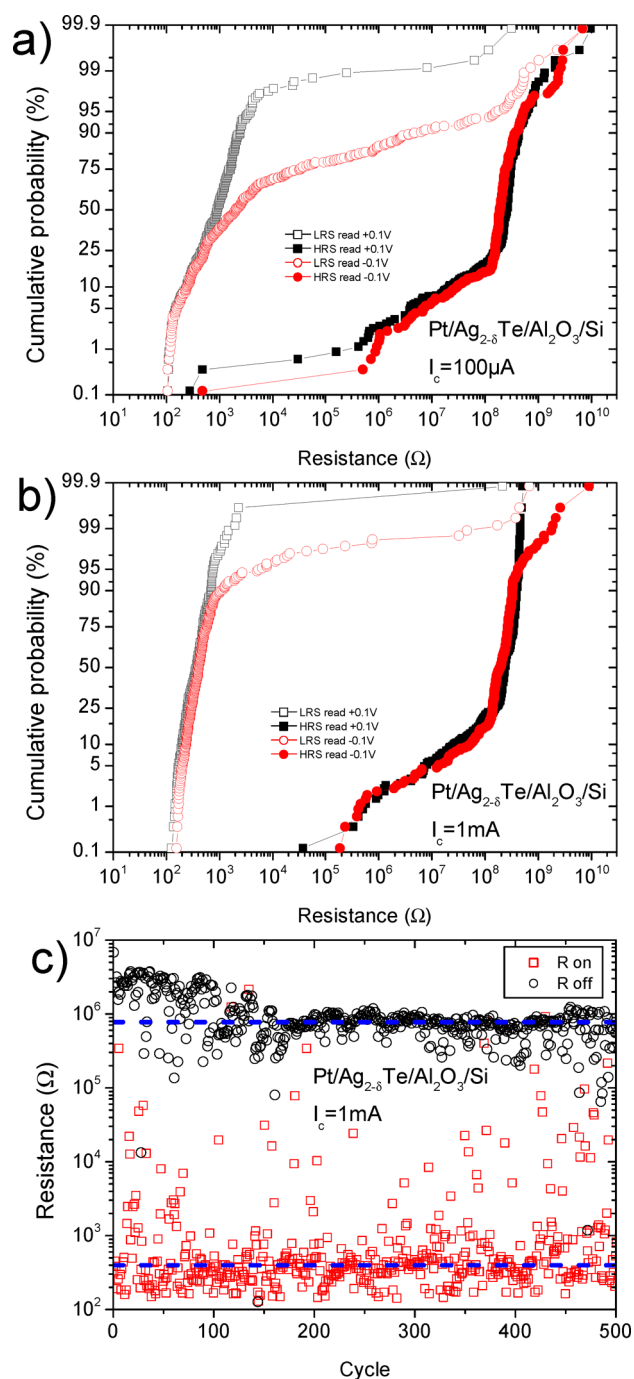
Figure 6. Cumulative distribution of HRS and LRS extracted from the set sweep (R at +0.1 V) or reset sweep (R at −0.1 V) of Pt/$Ag_{2-\delta}$Te/Al_2O_3/Si CBRAM cells cycled with a I_c of (a) 100 μA and (b) 1 mA. (c) Endurance test of a Pt/$Ag_{2-\delta}$Te/Al_2O_3/Si cell, showing the resistance extracted from a 100 mV read pulse after every set (R_{on}) or reset (R_{off}) sweep. The median LRS and HRS are indicated by the dashed line.

of the Te composition allowed us to investigate the phase stability of the formed phases and showed the occurrence of a melting point near 350 °C for more than 38 at% Te. The combined SEM and XRD data reveals only a narrow composition range between 33 and 38 at% Te, which shows suitable material properties for application as a cation supply layer in CBRAM. Resistive switching of Pt/$Ag_{2-\delta}$Te/Al_2O_3/Si CBRAM cells were investigated and compared to memory cells

with pure Ag as a cation supply layer. A more efficient reset for the Te alloyed cells was observed, which might be explained by the ionic conductive properties of the cation supply layer, allowing an efficient extraction of the cations out of the switching layer back to the supply layer. This enhanced reset might also be related to preferred formation of Ag−Te phases in the supply layer by expense of the Ag atoms constituting the conductive filament.

ASSOCIATED CONTENT

Ⓢ Supporting Information

Figure S1 showing in situ XRD patterns in the 10−30° window of a Ag−Te layer containing 63.9 at% Ag, Figure S2 showing SEM images of a 50 nm layer containing 64.8 and 70 at% Ag, and Figure S3 showing corresponding in situ XRD patterns of the Ag−Te layers in Figure S2. This material is available free of charge via the Internet at http://pubs.acs.org.

AUTHOR INFORMATION

Corresponding Author
*E-mail: Wouter.Devulder@UGent.be.

Notes
The authors declare no competing financial interest.

ACKNOWLEDGMENTS

REFERENCES

(1) Waser, R.; Dittmann, R.; Staikov, G.; Szot, K. Redox-based resistive switching memories—Nanoionic mechanisms, prospects, and challenges. *Adv. Mater.* **2009**, *21*, 2632−2663.

(2) Valov, I.; Waser, R.; Jameson, J. R.; Kozicki, M. N. Electrochemical metallization memories—Fundamentals, applications, prospects. *Nanotechnology* **2011**, *22*, No. 254003.

(3) Terabe, K.; Nakayama, T.; Hasegawa, T.; Aono, M. Ionic/electronic mixed conductor tip of a scanning tunneling microscope as a metal atom source for nanostructuring. *Appl. Phys. Lett.* **2002**, *80*, 4009−4011.

(4) Sakamoto, T.; Sunamura, H.; Kawaura, H.; Hasegawa, T.; Nakayama, T.; Aono, M. Nanometer-scale switches using copper sulfide. *Appl. Phys. Lett.* **2003**, *82*, 3032−3034.

(5) Kozicki, M.; Park, M.; Mitkova, M. Nanoscale memory elements based on solid-state electrolytes. *IEEE Trans. Nanotechnol.* **2005**, *4*, 331−338.

(6) Kund, M.; Beitel, G.; Pinnow, C.-U.; Rohr, T.; Schumann, J.; Symanczyk, R.; Ufert, K.-D.; Muller, G. Conductive bridging RAM (CBRAM): an emerging non-volatile memory technology scalable to sub-20-nm. *Technol. Dig., Int. Electron Devices Meet.* **2005**, 754−757.

(7) Wu, S.; Tsuruoka, T.; Terabe, K.; Hasegawa, T.; Hill, J. P.; Ariga, K.; Aono, M. A polymer-electrolyte-based atomic switch. *Adv. Funct. Mater.* **2011**, *21*, 93−99.

(8) Tada, M.; Okamoto, K.; Sakamoto, T.; Miyamura, M.; Banno, N.; Hada, H. Polymer solid-electrolyte switch embedded on CMOS for nonvolatile crossbar switch. *Electron Devices, IEEE Trans.* **2011**, *58*, 4398−4406.

(9) Wang, Y.; Lv, H.; Wang, W.; Liu, Q.; Long, S.; Wang, Q.; Huo, Z.; Zhang, S.; Li, Y.; Zuo, Q.; Lian, W.; Yang, J.; Liu, M. Highly stable radiation-hardened resistive-switching memory. *IEEE Electron Device Lett.* **2010**, *31*, 1470−1472.

(10) Tsuruoka, T.; Terabe, K.; Hasegawa, T.; Aono, M. Forming and switching mechanisms of a cation-migration-based oxide resistive memory. *Nanotechnology* **2010**, *21*, 425205.

(11) Liu, Q.; Long, S.; Wang, W.; Zuo, Q.; Zhang, S.; Chen, J.; Liu, M. Improvement of resistive switching properties in ZrO₂—Based

ReRAM with implanted Ti ions. *IEEE Electron Device Lett.* **2009**, *30*, 1335−1337.

(12) Schindler, C.; Weides, M.; Kozicki, M. N.; Waser, R. Low current resistive switching in Cu-SiO$_2$ cells. *Appl. Phys. Lett.* **2008**, *92*, No. 122910.

(13) Bernard, Y.; Renard, V. T.; Gonon, P.; Jousseaume, V. Back-end-of-line compatible conductive bridging RAM based on Cu and SiO$_2$. *Microelectron. Eng.* **2011**, *88*, 814−816.

(14) Goux, L.; Opsomer, K.; Degraeve, R.; Muller, R.; Detavernier, C.; Wouters, D. J.; Jurczak, M.; Altimime, L.; Kittl, J. A. Influence of the Cu-Te composition and microstructure on the resistive switching of Cu-Te/Al$_2$O$_3$/Si cells. *Appl. Phys. Lett.* **2011**, *99*, No. 053502.

(15) Aratani, K.; Ohba, K.; Mizuguchi, T.; Yasuda, S.; Shiimoto, T.; Tsushima, T.; Sone, T.; Endo, K.; Kouchiyama, A.; Sasaki, S.; Maesaka, A.; Yamada, N.; Narisawa, H. A novel resistance memory with high scalability and nanosecond switching. *Int. Electron Devices Meet.* **2007**, 783−786.

(16) Kim, S.; Jo, M.; Park, J.; Lee, J.; Lee, W.; Hwang, H. Forming-free CuC-buffer oxide resistive switching behavior with improved resistance ratio. *Electrochem. Solid-State Lett.* **2011**, *14*, 322−325.

(17) Devulder, W.; Opsomer, K.; Seidel, F.; Belmonte, A.; Muller, R.; de Schutter, B.; Bender, H.; Vandervorst, W.; van Elshocht, S.; Jurczak, M.; Goux, L.; Detavernier, C. Influence of carbon alloying on the thermal stability and resistive switching behavior of copper-telluride-based CBRAM cells. *ACS Appl. Mater. Interfaces* **2013**, *5*, 6984−6989.

(18) Radhakrishnan, H. Non-volatile and volatile bipolar resistive electrical switching in Ag and Cu chalcogenide memories with a dedicated switching layer. *15th IEEE Mediterranean Electrotech. Conf.* **2010**, 515−520.

(19) Yakshibaev, R. A.; Mukhamadeeva, N. N.; Almukhametov, R. F. Phase transformations and ionic transport in the Cu2-δTe superionic conductor. *Phys. Status Solidi A* **1988**, *108*, 135−141.

(20) Devulder, W.; Opsomer, K.; Franquet, A.; Meersschaut, J.; Belmonte, A.; Muller, R.; De Schutter, B.; Van Elshocht, S.; Jurczak, M.; Goux, L.; Detavernier, C. Influence of carbon content on the copper-telluride phase formation and on the resistive switching behavior of carbon alloyed Cu-Te conductive bridge random access memory cells. *J. Appl. Phys.* **2014**, *115*, No. 054501.

(21) Karakaya, I.; Thompson, W. The Ag-Te (silver-tellurium) system. *J. Phase Equilib.* **1991**, *12*, 56−63.

(22) *JCPDS Data Card No. 03-065-2871*; International Centre for Diffraction Data: Newtown Square, PA, 2004.

(23) *JCPDS Data Card No. 00-034-0142*; International Centre for Diffraction Data: Newtown Square, PA, 2004.

(24) *JCPDS Data Card No. 01-086-1953*; International Centre for Diffraction Data: Newtown Square, PA, 2004.

(25) *JCPDS Data Card No. 00-036-1452*; International Centre for Diffraction Data: Newtown Square, PA, 2004.

(26) *JCPDS Data Card No. 01-081-1822*; International Centre for Diffraction Data: Newtown Square, PA, 2004.

(27) *JCPDS Data Card No. 01-081-1821*; International Centre for Diffraction Data: Newtown Square, PA, 2004.

(28) Rom, I.; Sitte, W. Composition dependence of chemical diffusion coefficient and ionic conductivity of α'- and α-Ag2Te. *Solid State Ionics* **1994**, *70−71* (Part 1), 147−152.

(29) Bürgermeister, A.; Sitte, W. Chemical diffusion in β-Ag2Te. *Solid State Ionics* **2001**, *141−142*, 331−334.

(30) Billen, J.; Steudel, S.; Müller, R.; Genoe, J.; Heremans, P. A comprehensive model for bipolar electrical switching of CuTCNQ memories. *Appl. Phys. Lett.* **2007**, *91*, No. 263507.

(31) Mueller, R.; Genoe, J.; Heremans, P. Bipolar resistive electrical switching of silver tetracyanoquinodimethane based memory cells with dedicated silicon dioxide switching layer. *Appl. Phys. Lett.* **2009**, *95*, No. 133509.

(32) Guy, J. Investigation of the physical mechanisms governing data-retention in down to 10 nm nano-trench Al$_2$O$_3$/CuTeGe conductive bridge RAM (CBRAM). *IEEE Int. Electron Devices Meet.* **2013**, 30.2.1−30.2.4.